

High-Temperature Stability and Phase Transformations of Titanium Carbide ($\text{Ti}_3\text{C}_2\text{T}_x$) MXene

Brian C. Wyatt^{1,2†}, Srinivasa Kartik Nemani^{1,2†}, Krishay Desai¹, Harpreet Kaur¹, Bowen Zhang^{1,2}, Babak Anasori^{1,2*}

1. Department of Mechanical and Energy Engineering, Purdue School of Engineering and Technology, Indiana University-Purdue University Indianapolis, Indianapolis, IN 46202, USA
2. Integrated Nanosystems Development Institute, Indiana University-Purdue University Indianapolis, Indianapolis, IN 46202, USA

† contributed equally

* **Corresponding author:** Babak Anasori: banasori@iupui.edu

Abstract:

Two-dimensional (2D) transition metal carbides, nitrides, and carbonitrides, known as MXenes, are under increasing pressure to meet technological demands in high-temperature applications, as MXenes can be considered as one of the few high temperature 2D materials. Although there are studies on the stability of their surface functionalities, there is a gap in fundamental understanding of the phase stability and transformation of the metal carbide core at high temperatures ($> 700\text{ }^\circ\text{C}$) in an inert environment. In this study, we conduct systematic annealing of $\text{Ti}_3\text{C}_2\text{T}_x$ MXene films in which we present the 2D MXene flake phase transformation to ordered vacancy superstructure of a bulk three-dimensional (3D) Ti_2C phase and 3D bulk TiC_y crystals at $700\text{ }^\circ\text{C} \leq T \leq 1000\text{ }^\circ\text{C}$ with subsequent transformation to disordered carbon vacancy cubic TiC_y during annealing at higher temperatures ($T > 1000\text{ }^\circ\text{C}$). We annealed $\text{Ti}_3\text{C}_2\text{T}_x$ MXene films made from the delaminated MXene single-flakes as well as the multi-layer MXene clay powder in a controlled environment through the use of *in-situ* hot stage x-ray diffraction (XRD) paired with a 2D detector (XRD²) up to $1000\text{ }^\circ\text{C}$ and *ex-situ* annealing in a tube furnace and spark plasma sintering up to $1500\text{ }^\circ\text{C}$. Our XRD² analysis paired with cross-sectional scanning electron microscope imaging indicated the resulting nano-sized lamellar and micron-sized cubic grain morphology of the 3D crystals depend on the starting $\text{Ti}_3\text{C}_2\text{T}_x$ form. While annealing the multi-layer MXene create TiC_y grains with cubic and irregular morphology, the grains of 3D Ti_2C and TiC_y formed by annealing the $\text{Ti}_3\text{C}_2\text{T}_x$ MXene single-flake films keep the lamellar morphology. The ultrathin lamellar nature of the 3D grains formed at temperatures $>1000\text{ }^\circ\text{C}$ can pave way for applications of MXenes as a stable carbide material 2D additive for high-temperature applications.

Keywords: 2D materials, MXenes, high-temperature materials, carbides, phase transformation, XRD, phase stability, vacancy ordering

Introduction

Two-dimensional (2D) nanomaterials have become a widely studied family of materials in recent years due to their electrical conductivity [1] and high chemical activity [2], which has led them to be a highly competitive family of materials in the race for advancements in energy storage [3-5] and catalytic applications [6, 7]. In 2011, the 2D nanomaterials expanded to include a family of 2D transition metal carbides, nitrides, and carbonitrides commonly referred to as MXenes [8, 9]. MXenes are layered nanomaterials denoted by the chemical formula $M_{n+1}X_nT_x$, where M stands for 3d-5d block transition metals of groups 3-6 of the periodic table, X stands for carbon or nitrogen, and T_x stands for surface terminations such as $-O$, $-F$, $-Cl$, and $-OH$ [10, 11]. MXenes derive their hexagonal crystal structure with space group P63/mmc from their layered precursors MAX phases, where M and X layers are sandwiched by A-group element layers where the A-group layer is comprised of an element from groups 13-15 of the periodic table [12]. MXenes are derived from MAX phase precursors by selective removal of the A-group layer via selective wet chemical [9, 13, 14] or molten salt [11] etching methods. MXenes have grown to prominence in energy storage [15] and catalytic applications [16] due to their high electrical conductivity ($\sim 20,000 \text{ S}\cdot\text{cm}^{-1}$ in film form) [17], chemically active surfaces [18], high mechanical stiffness ($386 \pm 13 \text{ GPa}$ in $\text{Nb}_4\text{C}_3\text{T}_x$) [19, 20], and strong anchoring effect in hybridized materials [21, 22].

$\text{Ti}_3\text{C}_2\text{T}_x$ MXene, which is derived from the MAX phase Ti_3AlC_2 [8], has established itself as the most studied layered carbide from the MXene family [23]. It exhibits impressive material properties such as a high in-plane mechanical stiffness ($330 \pm 30 \text{ GPa}$) [19], high electrical conductivity ($10,000 - 20,000 \text{ S}\cdot\text{cm}^{-1}$) [17, 24], high colloidal stability (up to -40 mV in a range of solutions) [25, 26], and high temperature phase stability (up to $800 \text{ }^\circ\text{C}$ under inert environments) [27]. However, it is known that the exposure of $\text{Ti}_3\text{C}_2\text{T}_x$ to high temperatures in the presence of oxygen such as colloidal dispersions in aqueous media, or MXene films to air/moisture, exhibit variable rates of oxidation and degradation depending upon the net oxygen availability [28-31]. Although the formation of rutile and anatase phases of TiO_2 is beneficial to some extent in electrochemistry [32, 33] and catalysis [34] due to synergetic phasing between the oxide and carbon [16], the formation of oxides is less ideal for high-temperature applications of MXene which require retention of its high electrical and mechanical properties. Furthermore, high temperature synthesis of $\text{Ti}_3\text{C}_2\text{T}_x$ hybrids for energy storage or catalytic purposes has thus far not investigated the effect of synthesis temperatures [16] on the structure of $\text{Ti}_3\text{C}_2\text{T}_x$. More

recently, MXenes have been explored as a promising additive in metal and ceramic matrix composites, where processing at relatively high temperatures is required [35-38]. The addition of MXene flakes and particles as additive have exhibited improved in-matrix mechanical and electrical properties [25, 35, 37]. In general, any phase transformation that occurs due to high temperature annealing of $\text{Ti}_3\text{C}_2\text{T}_x$ in a non-oxidizing environment may have a large effect on the resultant electrical, catalytic, and mechanical properties, which could potentially affect the energy storage, catalytic potential, mechanical, and electrical properties of the hybrid or composite materials.

Early studies of the effect of high temperatures on $\text{Ti}_3\text{C}_2\text{T}_x$ films in low-oxygen environments has established a three-stage transformation process. Low temperature annealing up to $200 \text{ }^\circ\text{C}$ has seen the loss of water molecules trapped between the MXene layers [27, 39, 40]. This first stage is then followed by the desorption of functional groups dependent on the annealing temperature. Temperatures of $300\text{-}500 \text{ }^\circ\text{C}$ have been reported to result in the removal of $-OH$ groups. Further, $-F$ groups have been reported to desorb between $500 - 750 \text{ }^\circ\text{C}$ [39, 41] with complete desorption of all $-F$ and $-OH$ groups above $800 \text{ }^\circ\text{C}$ [39, 41, 42]. At temperatures above $800 \text{ }^\circ\text{C}$, phase transformation to cubic TiC_y has been reported, while full transformation of $\text{Ti}_3\text{C}_2\text{T}_x$ to cubic TiC_y was reported at temperatures of $1500 \text{ }^\circ\text{C}$ [27]. At the atomic level, in situ annealing of a single-flake of a $\text{Ti}_3\text{C}_2\text{T}_x$ in a scanning transmission electron microscope (STEM) showed the growth of MXene to thicker layers of Ti_4C_3 and Ti_5C_4 [43]. However, detailed characterization of this phase transformation of $\text{Ti}_3\text{C}_2\text{T}_x$ to TiC_y or other layered titanium carbide phases has yet to be completed.

Fundamentally, $\text{Ti}_3\text{C}_2\text{T}_x$ is a nano-lamellar titanium carbide, which means that $\text{Ti}_3\text{C}_2\text{T}_x$ has compositional similarity to the bulk crystalline three-dimensional (3D) nano-lamellar transition metal carbides that have been studied for the past > 50 years [44]. We can use previously established literature on the bulk carbides [45] as a guide on the potential phase transformation behavior of $\text{Ti}_3\text{C}_2\text{T}_x$ during high temperature annealing. Studies on cubic non-stoichiometric titanium carbide have identified the preference of titanium carbide to form the more stable formation of cubic TiC_y when TiC_y ($0.5 < y < 1.0$, where y represents the molar ratio of carbon to titanium), is annealed at temperatures below $800 \text{ }^\circ\text{C}$ [46, 47]. Until the discovery of MXenes, stable nano-lamellar formations of transition metal carbides had been observed only after long duration of annealing due to carbon vacancy ordering in transition metal carbides with structures such as M_3C_2 , and M_4C_3 [44, 48, 49]. Due to the low diffusive mobility of the carbon atoms, the

disordered state of the non-stoichiometric carbides (for example, TiC_y) are retained after cooling from the sintering temperatures which are at $T > 900\text{ }^\circ\text{C}$ [45].

The disorder to long-range ordered phase transformations of carbon vacancies in 3D bulk TiC_y at low carbon contents has been significantly explored in literature [46, 50, 51] from carbon contents ranging from $0.48 < y < 0.95$ [52]. The phase diagram of the Ti-C system is shown in Figure S1. Ordered carbon vacancy superstructure phases of TiC_y such as cubic and trigonal Ti_2C [53, 54], orthorhombic Ti_3C_2 [50], and hexagonal Ti_6C_5 [50, 55, 56], have been reported as stable phases of Ti-C during low temperature and long duration annealing ($\sim 620\text{-}760\text{ }^\circ\text{C}$) [45]. Although hexagonal Ti_6C_5 has been theoretically predicted for carbon contents ranging from $0.78 < y < 0.88$ [50, 51, 57], and experimentally reported in thin films [58], it has not been a widely reported phase in the Ti-C system. Similarly, while the formation of orthorhombic Ti_3C_2 for carbon contents ranging from $0.61 < y < 0.63$ has been reported by a several step annealing at temperatures $500\text{ }^\circ\text{C} < T < 800\text{ }^\circ\text{C}$ for 340 hours [50], it has not been confirmed by other groups experimentally [46, 50, 59]. However, many theoretical and experimental studies confirmed the formation of the carbon-vacancy ordered superstructure Ti_2C in both cubic and trigonal form [45-47, 54, 60, 61].

Bulk 3D crystalline trigonal Ti_2C is the most dominant superstructure of annealed TiC_y between carbon contents of $0.5 < y < 0.67$ [47, 52, 54] in a temperature range of $700 < T < 780\text{ }^\circ\text{C}$ [54, 62]. However, trigonal Ti_2C has been shown to be a long-term superstructure of TiC_y , where the cubic Ti_2C forms as a metastable phase [47]. Although Ti-C has the predefined preference toward cubic lattices, trigonal Ti_2C is reported to be more stable than cubic Ti_2C (+11.6 kJ/mole) as carbon vacancies slightly distort the cubic Ti_2C structure, which increases the effect of metallic bonding between the *d*-orbitals of Ti-Ti on the lattice. The carbon-vacancy ordered Ti_2C superstructure of both cubic and trigonal have similar X-ray diffraction (XRD) patterns, with a slight peak split at $\sim 76^\circ$ for the trigonal phase [45].

In general, previous studies on bulk non-stoichiometric phases reveal that formation of vacancy ordered nonstoichiometric phases require long annealing times at temperatures between 600-1000 $^\circ\text{C}$. For shorter annealing durations, Ti_2C has been shown to form simultaneously with TiC_y in Ti-C systems [61]. At temperatures beyond 1000 $^\circ\text{C}$, cubic TiC_y is the only remaining phase [45]. Therefore, we hypothesized that 2D $\text{Ti}_3\text{C}_2\text{T}_x$ MXene would have two main ranges of phase transition to bulk 3D crystalline titanium carbide phases: (1) Low temperature phase transition to a mix of 3D crystalline $\text{Ti}_2\text{C} + \text{TiC}_y$ at temperatures between 700 – 1000 $^\circ\text{C}$ followed by (2) high temperature phase

transition to purely TiC_y at temperatures above 1000 $^\circ\text{C}$. In this study, we have experimentally evaluated the phase transformation of 2D $\text{Ti}_3\text{C}_2\text{T}_x$ MXene films made from two different forms of MXenes derived in the wet chemical selective etching process: a) Non-delaminated multi-layer stacked of $\text{Ti}_3\text{C}_2\text{T}_x$ (referred to as clay) and b) delaminated single-to-few layers of flakes of $\text{Ti}_3\text{C}_2\text{T}_x$ (referred to as single-flake). To investigate the phase transformations of these forms of $\text{Ti}_3\text{C}_2\text{T}_x$, we used *in-situ* heated x-ray diffraction paired with a 2D detector (XRD²) (up to 1000 $^\circ\text{C}$) and *ex-situ* methods using tube furnace and spark plasma sintering (SPS) for high temperature annealing (up to 1500 $^\circ\text{C}$). The conductivities of the films were measured with a four-point probe system. This study details the effect of annealing on the inherent structure of $\text{Ti}_3\text{C}_2\text{T}_x$ to provide insight into the effect of high temperature synthesis of future MXene hybrids and composites for structural composite as well as energy storage and catalytic applications.

Methods

All powders used in this study, such as TiC (350 mesh-Fisher Scientific) Al (350 mesh-Fisher Scientific), C (calcinated coke-Fisher Scientific) LiCl (Fisher), are used without any further processing. Hydrochloric acid (HCl, 37%) and hydrofluoric acid (HF, 48%) were procured from Fisher Scientific. De-oxygenated deionized water (DO) was prepared in-house by Ar bubbling de-ionized (DI) water for 10-15 min.

MAX Synthesis

Ti_3AlC_2 MAX phase was synthesized by tumbler milled mixing TiC, Al, C powders in powder ratios of 1:1:1 for 18 h at 60 RPM [14]. Mixed powders were sintered in a tube furnace (Carbolite Gero) at 1415 $^\circ\text{C}$ for 2 h under constant Ar flow. In a typical synthesis, 30 g of mixture was sintered to yield a brick (28.5-29 g) of Ti_3AlC_2 . Fine powders were obtained by drilling the brick with a titanium nitride coated drill bit.

MXene Synthesis

MXene was synthesized by etching 4 g of Ti_3AlC_2 MAX powder in 36 ml DI water, 12 ml HF (48%) and 72 ml HCl (37%) in a heated oil bath at 35 $^\circ\text{C}$ for 24 h with constant stirring at 300 RPM. MAX powder was gradually added to the polycarbonate cylindrical bottle (250 ml) containing the aqueous etchant solution at room temperature and then the solution was set at 35 $^\circ\text{C}$ [63]. All etching steps were performed in a fume hood.

The etched MAX phase with acidic solution was decanted after 24 h, washed repeatedly (typically with 250 ml of DI water) in a centrifuge at 4200 RPM (3320 RCF) for 5-10 min to neutralize the pH. The wet etched MXene was then transferred to a new polycarbonate cylindrical bottle with 4 g LiCl dissolved in 200 ml DO water and stirred at 65 $^\circ\text{C}$ for 2 h under constant Ar flow. The intercalated solution was then repeatedly washed (typically with 250-300 ml) DO water to remove the salt, at 14,000 RPM (22,830 RCF) in a centrifuge with gradually increasing times 10-30 min for subsequent runs up to three cycles. We ran the third centrifuge cycle for 30 min and collected the resulting supernatant ($\sim 5\text{ mg}\cdot\text{mL}^{-1}$) which we

vacuum filtered on a 0.8- μm -pore size mixed cellulose ester membrane filter paper to make our delaminated flake $\text{Ti}_3\text{C}_2\text{T}_x$ films (referred to as single-flake $\text{Ti}_3\text{C}_2\text{T}_x$ films). We also filtered the sediment of the same centrifuge cycle by adding ~ 10 mL of DI water and vacuum filtration to make our clay $\text{Ti}_3\text{C}_2\text{T}_x$ films. The film thicknesses were in the range of 60–100 μm . After the filter paper was removed, each film was then dried in a vacuum oven at 150 $^\circ\text{C}$ overnight to remove the intercalated water molecules between layers of $\text{Ti}_3\text{C}_2\text{T}_x$ before high temperature annealing.

In-Situ Hot Stage Two-Dimensional X-ray diffraction (XRD²)

$\text{Ti}_3\text{C}_2\text{T}_x$ clay and single-flake films were cut into 5 mm x 10 mm rectangular pieces and then two or three of these film pieces were stacked on an AlN substrate in an Anton-Parr DHS 1100 Domed Hot Stage. The films were then secured to the AlN substrate using two 316L stainless steel clips at on the short edges of the film. The sample height was then aligned using dual focused laser beams. Our XRD setup was considered focused when these dual beams were concentric. In order to verify that AlN was not detected in addition to the diffraction signal from our stacked $\text{Ti}_3\text{C}_2\text{T}_x$ film samples, an XRD scan from 5 – 75 $^\circ$ (2 θ) (full spectrum of 0 $^\circ$ - 90 $^\circ$ 2 θ) was captured using a Bruker D8 Discover x-ray diffractometer paired with a Vantec XRD² detector using a Cu K α emitter with $\lambda \approx 1.5418$ Å using a step size of 5 $^\circ$ (2 θ) with a timestep of 20 s. After verification that no AlN signal was present, each sample was then covered using a graphite dome and set under a constant flow of Ar (99.998%) at an outlet pressure of 50 kPa. After setup, the hot stage was set to a constant 40 $^\circ\text{C}$ (considered scanning room temperature (RT), ambient RT in the room fluctuated around 35 $^\circ\text{C}$) and scanned from 5 – 75 $^\circ$ (2 θ) (full spectrum of 0 $^\circ$ - 90 $^\circ$ 2 θ) using a step size of 5 $^\circ$ (2 θ) with a timestep of 45 s (total 11 minutes scan). After this scan, the sample was then heated to a temperature between 600 – 1000 $^\circ\text{C}$ and held for 2 h. The sample was scanned using the same parameters as the 40 $^\circ\text{C}$ scan over this 2 h period, beginning once the stage reached temperature (called 0 Min) and ending at 2 h (called 105 Min). Between each scan, a 4-minute delay was used to reach a total of eight 15-minute scan segments. After heating, the sample was then allowed to cool to room temperature under forced convection via running air over the graphite dome to a safer temperature of 200 $^\circ\text{C}$, then the setup was allowed to reach RT at 40 $^\circ\text{C}$ via natural convection. After the sample was cooled to RT, the Ar gas was turned off and the graphite dome was removed.

$\text{Ti}_3\text{C}_2\text{T}_x$ MXene clay and single-flake films post-annealing in the hot stage were prepared for XRD² via placement on double-sided amorphous carbon tape on glass slides. XRD² scans were conducted from 5 – 75 $^\circ$ (2 θ) (full spectrum of 0 $^\circ$ - 90 $^\circ$ 2 θ) using a step size of 5 $^\circ$ (2 θ) with a timestep of 45 s (total 11 minutes scan).

In addition to our experiments, the accuracy of the peak positions of our XRD² scans was evaluated using an Al_2O_3 corundum standard. These results were then compared to online crystallography database spectrums for corundum standards in Figure S2.

Spark Plasma Sintering (SPS) and tube furnace annealing of $\text{Ti}_3\text{C}_2\text{T}_x$ MXene films

$\text{Ti}_3\text{C}_2\text{T}_x$ MXene clay and single-flake films were cut into 5 mm x 5 mm square pieces and were laid flat between two 20 mm polished tungsten discs (top and bottom). We also put a 1-mm-

thick grafoil disc as a spacer between the tungsten discs in which we cut a square opening of 7 x 7 mm, where we put in the MXene film. The two discs containing the $\text{Ti}_3\text{C}_2\text{T}_x$ films in the SPS graphite dies, and the graphite dies were lined with a 0.005 in grafoil sheets and a thin disc of grafoil was added to the top and bottom punches.

Sample die was pressed manually to ensure the setup was rigid with no moving parts and was pressed with a 6 MPa pressure with a ramp rate of 10 MPa/min and heated to 900, 1200, and 1500 $^\circ\text{C}$ at a rate of 60 $^\circ\text{C}/\text{min}$ in a SPS machine (Thermal Technology-DCS 10). A constant He flow (1 L/min) was maintained throughout the run. The holding time was set at 1 h with the pressure held constant throughout the run. The die was allowed to cool to room temperature before the pressure was removed and the samples were taken out.

Tube furnace annealing was carried out using a Carbolite Gero tube furnace. Small pieces of $\text{Ti}_3\text{C}_2\text{T}_x$ single-flake and clay film samples were cut in 1 x 1 cm squares and stacked in 3 - 4 layers. These stacked films were then placed into a graphite crucible between 3 - 4 layers of 0.005 in grafoil sheets on either side. The $\text{Ti}_3\text{C}_2\text{T}_x$ single-flake and clay film samples were then subsequently annealed at 800 $^\circ\text{C}$ for 18 h under inert gas flow with a heating ramp rate of 3.5 $^\circ\text{C}/\text{min}$. After annealing, the film samples were then left in the furnace to cool under flowing inert gas to the ambient temperature.

SEM and EDS Characterization

A JEOL JSM-7800F FESEM equipped with an in-lens thermal field emission electron gun and a conical objective lens with in-tandem upper and lower electron detectors was used to collect morphological and compositional data of the samples. All specimens were sputter coated with gold (Denton Desk V Turbo) to enhance electron conduction on the surface. Energy Dispersion Spectroscopy (EDS) was performed via an EDAX Octane Super Detector and associated EDAX TEAM software.

Conductivity measurements

Sheet resistances of the MXene films were measured using a 4-point probe method with readings taken from a Keithley-2400 source meter. A minimum of 5 readings was taken across the film at various points to obtain an average value of the sheet resistance. All conductivity experiments were conducted in ambient air conditions at a room temperature of 24 $^\circ\text{C}$. Conductivities of the thin films were calculated from the bulk resistivities of the thin films.

Results & Discussion

To study the effect of MXene morphology on high temperature annealing we used two types of $\text{Ti}_3\text{C}_2\text{T}_x$ forms, single-flake vs. clay films (Figure 1), as the details were mentioned in the Methods section. Figure 1a shows a unit cell schematic of Ti_3AlC_2 MAX phase, which is then synthesized to $\text{Ti}_3\text{C}_2\text{T}_x$ MXene via wet chemical selective etching, where $\text{Ti}_3\text{C}_2\text{T}_x$ derives its nano-lamellar hexagonal crystal structure from its Ti_3AlC_2 precursor. The *a*-lattice parameter (*a*-LP) of the Ti_3AlC_2 MAX and the resulting $\text{Ti}_3\text{C}_2\text{T}_x$ MXene are similar (Figure 1a). However, the *c*-lattice parameter (*c*-LP) of $\text{Ti}_3\text{C}_2\text{T}_x$ can be larger than that of the Ti_3AlC_2 depending on the intercalated species [64]. At the end of

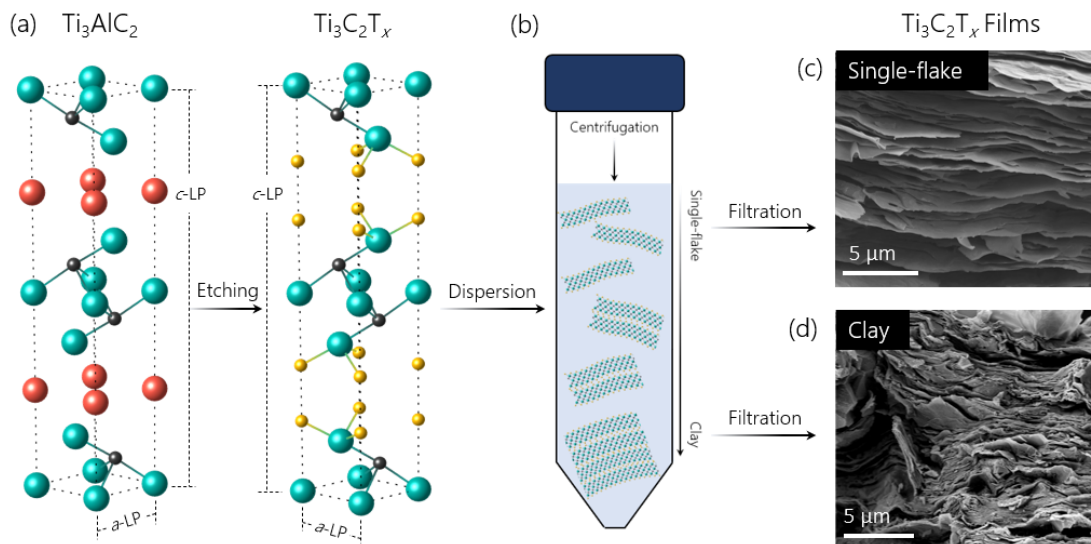


Figure 1. (a) $\text{Ti}_3\text{C}_2\text{T}_x$ derives its hexagonal close-packed structure through selective etching of its Ti_3AlC_2 precursor. (b) The $\text{Ti}_3\text{C}_2\text{T}_x$ is then separated by flake morphology through centrifugation into single-flake and clay $\text{Ti}_3\text{C}_2\text{T}_x$. The blue, black, red, and yellow atoms refer to Ti, C, Al, and T_x (-O, -F, -Cl, -OH), respectively. Single-flake (c) and clay (d) $\text{Ti}_3\text{C}_2\text{T}_x$ films were made by vacuum filtration of the $\text{Ti}_3\text{C}_2\text{T}_x$ solution. (c) Cross section SEM image of $\text{Ti}_3\text{C}_2\text{T}_x$ single-flake film made by filtration of the supernatant of the last centrifuge step (b) containing single-flake MXenes. (d) Cross section SEM image of the $\text{Ti}_3\text{C}_2\text{T}_x$ clay film made by vacuum filtration of the sediment of the last centrifugation step shown in (b).

selective etching and intercalation/delamination (see Methods section), the centrifuge tube of $\text{Ti}_3\text{C}_2\text{T}_x$ consists of supernatant and sediment. The supernatant contains the single-flake MXenes and the sediment is the clay containing stacks and particles of multi-layer MXenes (Figure 1b) as discussed in detail earlier [14]. The aqueous colloidal solutions of both clay and single-flake $\text{Ti}_3\text{C}_2\text{T}_x$ MXene were vacuum filtered to obtain films with thicknesses of 60-100 μm (Figure 1c and d). The morphology of clay is highly irregular with stacks of disordered $\text{Ti}_3\text{C}_2\text{T}_x$ particles and flakes in comparison to the neatly ordered morphology of single-flake $\text{Ti}_3\text{C}_2\text{T}_x$ films. We annealed both types of films at temperatures ranging from 600° to 1500 °C for different durations as discussed in the following sections of this paper.

Figure 2 shows the diffraction patterns of annealed $\text{Ti}_3\text{C}_2\text{T}_x$ from temperatures of 600 -1000 °C for both single-flake and clay films of $\text{Ti}_3\text{C}_2\text{T}_x$ for 2 hours under Ar flow using an *in-situ* hot stage XRD². A XRD plot of the precursor Ti_3AlC_2 MAX phase can be seen in Figure S3 for comparison purposes. Figure 2a bottom pattern shows the XRD² of the single-flake $\text{Ti}_3\text{C}_2\text{T}_x$ film annealed in a vacuum oven at 150 °C overnight as our control sample. In this sample's pattern, the (002) plane can be seen at 8.50° (2 θ), which is followed by subsequent (004), (006), (008), and (0010) reflections, respectively. These peaks correspond to a c-LP of 20.8 Å, which shows for most of the $\text{Ti}_3\text{C}_2\text{T}_x$ flakes almost all

the intercalated species are removed after annealing at 150 °C. However, there is a shoulder peak at 6.55°, which indicates that we still have some structural water molecules in between some of the MXene flakes. The peaks at 60.77° and 75.70° corresponds to the (110) and (205) planes, respectively, that are visible because of our 2D detector in XRD². The single-flake film annealed at 600 °C for 2 h shows slight shifting of the (002), (004), (006), (008), (0010), and (205) peaks due to the complete removal of intercalated species as previously reported [27, 39]. These XRD² pattern of the single-flake $\text{Ti}_3\text{C}_2\text{T}_x$ film annealed at 600 °C do not show the formation of new phases.

However, through increasement of the annealing temperature to 700 °C, the (00 l) peak intensities of $\text{Ti}_3\text{C}_2\text{T}_x$ decrease as new peaks start to appear while the (00 l) peaks positions do not shift and stay within less than 0.1° (2 θ). After annealing the single-flake $\text{Ti}_3\text{C}_2\text{T}_x$ film at 700 °C for 2 h, the peaks around 17.6° and 35.9° appear to have shoulders on their right-hand side (Figure 2a). The XRD² patterns in Figure S4 shows these shoulders more clearly. We can confirm that these shoulders in the XRD² pattern of the single-flake after annealing are new peaks as they do not follow the c-LP calculated from the (002) peak of the 700 °C annealed single-flake $\text{Ti}_3\text{C}_2\text{T}_x$ films. Based on the (002) peak position of the 700 °C sample, the expected higher order (004) plane can be seen at ~17.7° peak marked by blue

diamonds in Figure 2a 700 °C. Therefore, the appearance of these shoulders indicate that a new phase is forming. It is well-established that cubic TiC_y phases have a peak ~ 36.0 (2 θ) [45] while bulk 3D crystals of Ti_2C superstructure have a peak at $\sim 17.9^\circ$, which can correspond to the (111) peak of cubic or trigonal Ti_2C [50]. These shoulders in the (004) and (008) $Ti_3C_2T_x$ peaks correspond roughly to peak positions of 17.9° and 36.3° (2 θ), which we correspond to the formation of (111) plane of Ti_2C and the (111) plane of TiC_y phases, respectively. The formation of the (111) plane of Ti_2C during annealing at 700 °C simultaneously with TiC_y is expected, as Ti_2C is a superstructure of ordered vacancy TiC_y at 700 °C [50]. In addition, we speculate that this formed Ti_2C crystalline phase is likely cubic as phase transformation from cubic Ti_2C to trigonal Ti_2C is a slower transition. For example, in one study cubic Ti_2C was annealed for 10 days between 750 - 780 °C before trigonal Ti_2C was formed [54]. Therefore, early phase formation of the Ti_2C superstructure in the Ti-C system would be expected to be cubic Ti_2C . In addition, we analyzed our spectra for any formation of 3D bulk orthorhombic Ti_3C_2 superstructure, as it is predicted to form in the non-stoichiometric phase diagram [45] (Figure S1). However, orthorhombic Ti_3C_2 has its main

peak (111) at 19° (2 θ) [45] that we do not observe in any of our XRD patterns. The lack of this peak (111) at 19° (2 θ) indicates that only cubic Ti_2C and TiC_y are formed in our annealing process.

At higher temperatures ($\geq 800^\circ C$), peaks between $17.8 - 17.9^\circ$ as well as $36.0 - 36.2^\circ$ and $77.0^\circ - 77.20^\circ$ (2 θ) become dominant, which we can correspond to indication of (111) Ti_2C superstructure and (111) and (222) diffraction peaks of cubic TiC_y [45, 50], respectively. At these higher temperatures, we can still see the presence of the (004) and (008) peaks of $Ti_3C_2T_x$ in the shoulders of the (111) Ti_2C and (111) TiC_y peaks, respectively, on the left-hand side of each peak (Figure 2a). The strong intensity of the (111) diffraction peaks of Ti_2C and the (111) and (222) diffraction peaks of TiC_y at temperatures above 800 °C indicates that Ti_2C and TiC_y become the dominant phases during higher temperature annealing of single-flake $Ti_3C_2T_x$ films.

Interestingly, we do not see the clear formation of the other peaks of 3D crystalline Ti_2C or TiC_y , notably the intense (200), (220), or (311) peaks of TiC_y [45] (see the 1000 °C pattern in Figure 2a). A lack of clear formation of these peaks could be attributed to the in-plane ordering of nano-lamellar $Ti_3C_2T_x$ and its structural comparability

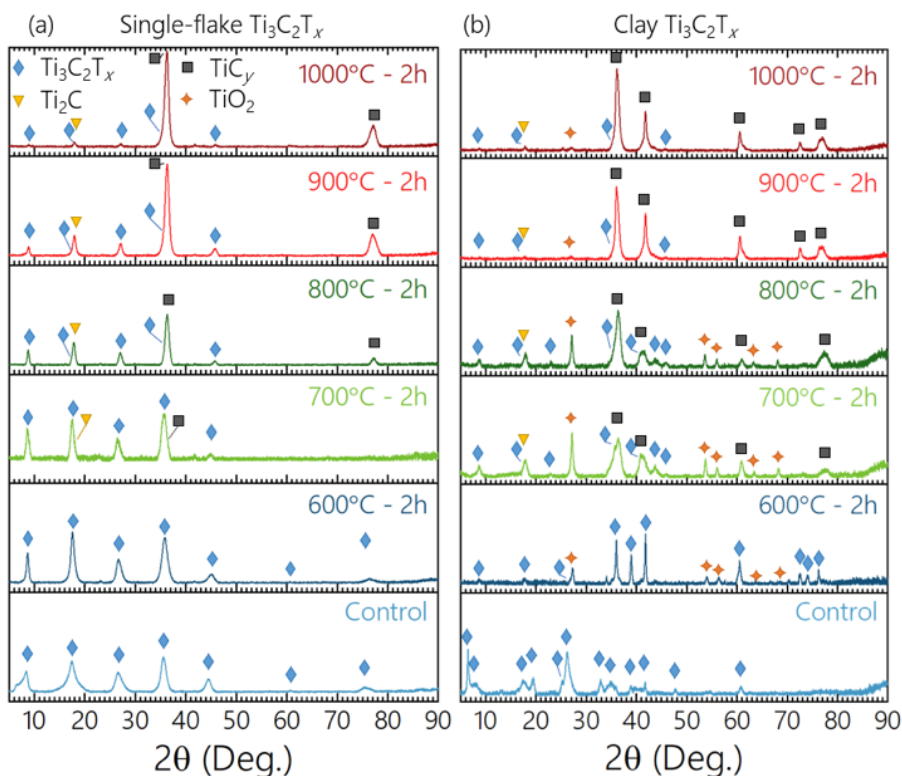


Figure 2. 2D XRD (XRD²) patterns of single-flake (a) and clay (b) $Ti_3C_2T_x$ films annealed at 600 °C to 1000 °C for 2 hours under Ar. The bottom patterns in both panels (marked as control) are the XRD² patterns of the as filtered films and vacuum annealed at 150 °C overnight to remove the intercalated water.

to the formed 3D crystalline Ti_2C and TiC_y phases. In cubic Ti_2C and TiC_y systems, the perspective of the cubic (111) plane is similarly ordered to the (00 l) plane of hexagonal $\text{Ti}_3\text{C}_2\text{T}_x$ MXene, with ordered stacking of Ti and C layers. The strong (111) diffraction signals of cubic Ti_2C and TiC_y suggests that Ti_2C and TiC_y preferentially form along the (00 l) plane of $\text{Ti}_3\text{C}_2\text{T}_x$ due to the closely related atomic packing. At 1000 °C, the peaks of $\text{Ti}_3\text{C}_2\text{T}_x$ are near non-existent, which suggests that temperatures of 1000 °C could be sufficient to form entirely lamellar TiC_y and Ti_2C along the original basal plane of $\text{Ti}_3\text{C}_2\text{T}_x$ in film form.

The $\text{Ti}_3\text{C}_2\text{T}_x$ control clay film XRD² pattern, displayed as the bottom pattern in Figure 2b, illustrates the disorder of the clay films as compared to the single-flake films. The control clay film which was annealed under vacuum at 150 °C for 18 h, showed two (002) peaks, 1) a sharp peak at 6.46° and 2) a broad peak at 8.39°. The sharp (002) peak at 6.46° has subsequent basal (006), (008), (0010) peaks as well as in-plane (106), (107), (110) peaks. The broad (002) peak at 8.39° has subsequent basal (004), (006), (008) peaks as well as in-plane (104) and (108) peaks. This mix of stackings of (00 l) peaks show the incomplete removal of the intercalated species (for example, water), and the visible in-plane peaks of $\text{Ti}_3\text{C}_2\text{T}_x$ [65] supports the conclusion of the disordered structure of clay $\text{Ti}_3\text{C}_2\text{T}_x$ films. In the annealed $\text{Ti}_3\text{C}_2\text{T}_x$ clay film at 600 °C, we observe the (002), (004), (006), (101), (102), (103), (104), (105), (110), (203), (204), and (205) peaks of $\text{Ti}_3\text{C}_2\text{T}_x$. Because of the disordered structure and the presence of two sets of $\text{Ti}_3\text{C}_2\text{T}_x$ peaks, we did not compare the peak positions directly to the control $\text{Ti}_3\text{C}_2\text{T}_x$ clay film (Figure S5). However, we can analyze the newly formed diffraction peaks corresponding to the (200) and (311) planes of TiC_y in our samples annealed from 700 – 1000 °C. In 700-1000 °C samples, we see new peaks corresponding to the (111) and (222) planes of TiC_y at 36.3° and 77.4°, respectively, as well as peaks corresponding to the (111) of Ti_2C superstructure at 17.9°, similar peaks to our single-flake films.

We also see peaks of rutile TiO_2 which appeared due to the *in-situ* annealing setup. However, this is likely due to a surface oxidation effect of partially present oxygen in the environment in our *in-situ* XRD² annealing setup. To confirm TiO_2 is only a surface oxidation, we used a Scotch tape method to peel the surface layers of these films followed by SEM on the newly exposed surfaces of the films. Our SEM and EDS results indicated significantly lower oxygen content in the central layers (Figure S6), which indicates that TiO_2 has only formed at the top surface layers. Regardless, our $\text{Ti}_3\text{C}_2\text{T}_x$ clay film also showed a new peak corresponding to the TiC_y (200) planes at 41.30° in the 700-800 °C and a new peak

corresponding to the (311) plane at 72.5° in the 900-1000 °C samples.

Although we would expect the in-plane peaks of disordered $\text{Ti}_3\text{C}_2\text{T}_x$ clay film to shift due to the change in the *c*-LP during the loss of intercalated water [27, 39], we can separate these in-plane peaks of $\text{Ti}_3\text{C}_2\text{T}_x$ from the peaks of the newly formed TiC_y phase. Specifically, the nearest in-plane peaks for the 700 °C and 800 °C samples would correspond to the (105) and (106) planes of $\text{Ti}_3\text{C}_2\text{T}_x$, which are located at 40.92° and 43.65° in these samples, respectively, and can be identified on the 700 °C and 800 °C spectra in Figure 2b with other $\text{Ti}_3\text{C}_2\text{T}_x$ peaks marked with blue diamonds. This supports that the strong 41.73° peak is likely the (200) peak of TiC_y , which would illustrate the formation of non-planar cubic TiC_y formation with respect to the (00 l) plane of $\text{Ti}_3\text{C}_2\text{T}_x$ in the clay film. In addition, while all the $\text{Ti}_3\text{C}_2\text{T}_x$ peaks almost disappear at > 900 °C, an intense peak at 72.5° appear which can correspond to the (311) plane of TiC_y , which further supports the formation of non-planar cubic TiC_y . The formation of non-planar cubic structures in annealed clay $\text{Ti}_3\text{C}_2\text{T}_x$ is in the contrast to the heat treated single-flake $\text{Ti}_3\text{C}_2\text{T}_x$ film, where we observed only certain planes and preferred orientation growth. This morphology dependent formation of TiC_y in $\text{Ti}_3\text{C}_2\text{T}_x$ single-flake and clay films was observed to be present in samples annealed in a tube furnace for 18 h (Figure S7). The appearance of different peaks of TiC_y illustrates that the morphology of $\text{Ti}_3\text{C}_2\text{T}_x$ MXene used in high temperature applications will impact the grain type of cubic structures formed as a product of annealing.

After careful analysis of the present phases in our samples using our XRD² scans of both annealed $\text{Ti}_3\text{C}_2\text{T}_x$ single-flake and clay films, we analyzed the structural characteristics of the newly formed Ti_2C and TiC_y phases, as shown in Figure 3. SEM images indicate that the cross section of annealed $\text{Ti}_3\text{C}_2\text{T}_x$ single-flake films remain lamellar in nature even after annealing at 1000 °C for 2 h, as shown in Figure 3a. As Figure 2 illustrated low signals of $\text{Ti}_3\text{C}_2\text{T}_x$ in single-flake films annealed at 1000 °C as compared to the signal from Ti_2C and TiC_y , these lamellar sheets shown in the cross-section SEM are most likely lamellar formations of 3D crystalline Ti_2C and TiC_y , as presented in the schematic in Figure 3a. Once annealed at high temperatures (for example, at 1000 °C), the disordered $\text{Ti}_3\text{C}_2\text{T}_x$ clay film illustrates formation of mostly bulk crystals of TiC_y spaced by lamellar formations of TiC_y (Figure 3b) [66]. Our EDS results indicated that these crystals were not oxides or intercalation salts (Figure S8), further confirming that they are carbide crystals. It was shown previously that high magnification SEM image of a bulk grain of TiC_y can be used to visualize the crystal planes of the formed TiC_y crystals [66]. The visualization of micron-sized

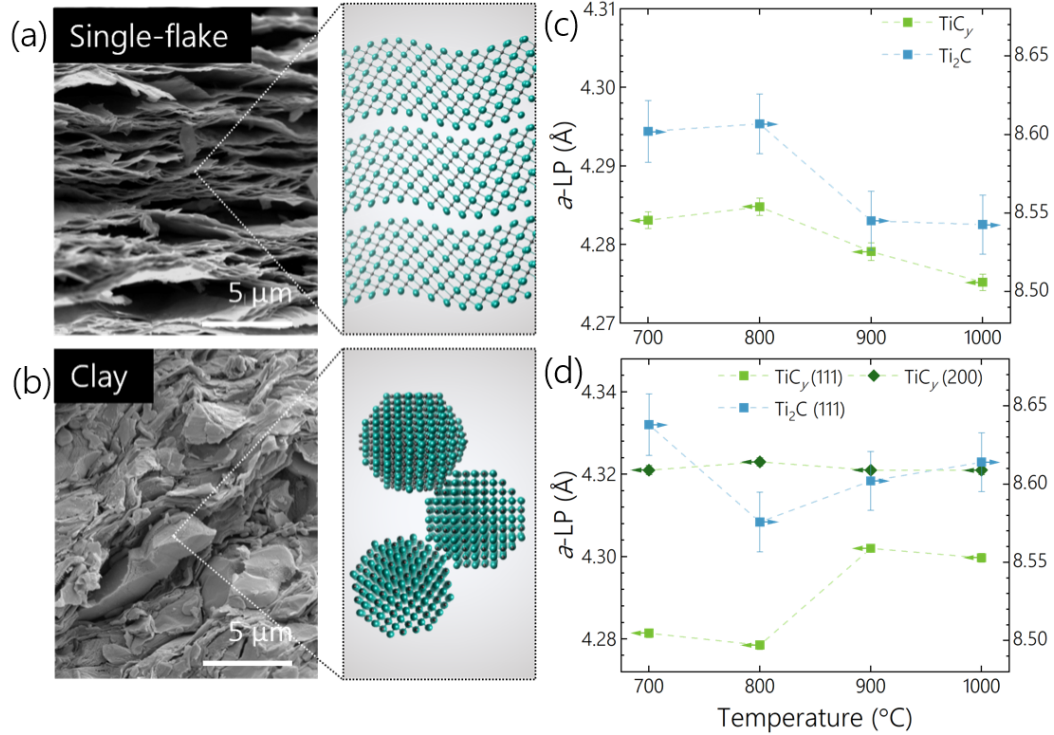


Figure 3. Structural characteristics of annealed $\text{Ti}_3\text{C}_2\text{T}_x$ MXene films in single-flake film and clay film forms from temperatures of 700°C - 1000°C. (a) and (b) cross-section SEM images of single-flake and clay $\text{Ti}_3\text{C}_2\text{T}_x$ MXene films annealed at 1000 °C for 2 hours. The carbide 3D structures formed after annealing of the single-flake keep their layered morphology as shown in the schematic, while the 3D carbide crystals formed from the annealed clay films have cubic irregular morphology in addition to the layered form. (c) and (d) the a -LPs of the cubic TiC_y and the cubic Ti_2C superstructure phases formed by annealing the single-flake films (c) and the clay film (d). The a -LPs were calculated from the XRD patterns conducted at room temperature (24 °C) after the annealing process.

crystals of TiC_y only in $\text{Ti}_3\text{C}_2\text{T}_x$ clay film annealed at 1000 °C suggests that the bulk TiC_y crystals have no preferred orientation and have irregular morphology of the multi-layer $\text{Ti}_3\text{C}_2\text{T}_x$ in the clay films.

We next investigated the structural parameters of the annealed single-flake and clay films (Figure 3c-d). To analyze the structure of the lamellar formation of Ti_2C and TiC_y from the annealed $\text{Ti}_3\text{C}_2\text{T}_x$ films, we focused on an analysis of the a -LPs in Figure 3c-d to provide evidence of stable distribution of carbon vacancies within the formed cubic structures. As previously reported, the a -LP of TiC_y increases by increasing the y ratio (carbon content) in the cubic Ti-C lattice [57]. For example, at 4.305 Å the a -LP of $\text{TiC}_{0.5}$ is slightly smaller than that of $\text{TiC}_{0.7}$ at 4.325 Å [45, 57]. Additionally, ordering of the carbon atoms results in slightly larger lattice parameters in TiC_y [57]. The slight increase of the a -LP between annealing temperatures of 700 °C and 800 °C could be due to the loss of the -OH and -F surface terminations of $\text{Ti}_3\text{C}_2\text{T}_x$ [27, 39, 41, 42]. However, the decreased a -LPs of both Ti_2C and TiC_y at temperatures of 900 °C to 1000 °C can be explained by carbon atoms

leaving the lamellar structure at temperatures > 900 °C as shown previously [27] which results in 3D crystals with lower Ti:C ratios. The different trend in the a -LP for $\text{Ti}_3\text{C}_2\text{T}_x$ clay films annealed between 900 – 1000 °C could be due to the multilayered nature of the clay $\text{Ti}_3\text{C}_2\text{T}_x$ films as compared to the single-flake films, as the clay forms larger cubic crystals in the film structure with a -LPs closer to the previously reported bulk TiC_y [57, 66].

Interestingly, when we analyze the a -LPs of the clay $\text{Ti}_3\text{C}_2\text{T}_x$ films annealed at 700 - 1000 °C based on the (200) peak, we attain an a -LP between 4.321 - 4.323 Å as shown in Figure 3d, which matches more closely to the published a -LPs of TiC_y . The smaller a -LPs of TiC_y as calculated by the (111) peak as compared to a -LPs calculated by the (200) peak in annealed clay $\text{Ti}_3\text{C}_2\text{T}_x$ films could be attributed to the lamellar formation of TiC_y in the (111) plane along the basal plane of $\text{Ti}_3\text{C}_2\text{T}_x$ MXene. As shown in Figure 2, peaks attributable to $\text{Ti}_3\text{C}_2\text{T}_x$ can still be seen up to 1000 °C indicating that the basal plane of the annealed flakes is simultaneously occupied by $\text{Ti}_3\text{C}_2\text{T}_x$ and TiC_y , which has been seen

previously in *in-situ* scanning transmission electron microscopy (STEM) studies [43]. The bond lengths of Ti-C in $\text{Ti}_3\text{C}_2\text{T}_x$ is reported to be 2.04 Å and 2.21 Å [67]. These differ from cubic TiC_y , where the bond length is reported to be 2.186 for stoichiometric $\text{TiC}_{1.0}$ [68]. The difference in bond lengths between simultaneously present $\text{Ti}_3\text{C}_2\text{T}_x$ and TiC_y in the lamellar structure could provide strain on the bonds between Ti-C in TiC_y , which may explain the slight difference in the *a*-LPs as calculated by the (111) peak of TiC_y as compared to the previous literature [69]. A similar strain on the Ti-C bonds in $\text{Ti}_3\text{C}_2\text{T}_x$'s structure as compared to the Ti-C bonds in TiC_y has been observed experimentally in recent studies on bare and functionalized $\text{Ti}_3\text{C}_2\text{T}_x$ [70]. Therefore, if it is strain on the Ti-C bonds that affects the *a*-LP as calculated by the (111) peak, the lack of this strain in the *a*-LP of the out-of-plane growth of 3D TiC_y crystals in the annealed clay $\text{Ti}_3\text{C}_2\text{T}_x$ would then be expected, as these grains would not have the same lamellar structural strain as the 2D formed TiC_y crystals. Size of the formed grains of in-plane and out-of-plane growth of TiC_y and Ti_2C was not conducted in this study, however, we believe that future high-resolution TEM studies could be used to visualize the effects and sizes of the grown grains of TiC_y and Ti_2C on the MXene structure. In general, we found that annealing temperatures of 700 – 1000 °C of the clay $\text{Ti}_3\text{C}_2\text{T}_x$ MXene films for 2 h is not substantial to form large 3D grains of cubic TiC_y crystals as the singular present phase. Therefore, we utilized *ex-situ* methods with spark plasma sintering to reach temperatures as high as 1500 °C to characterize the effect of higher temperatures on the phase transformation of $\text{Ti}_3\text{C}_2\text{T}_x$ to 3D crystals of TiC_y .

In our *ex-situ* high temperature experiments, we studied the crystal growth and phase change of $\text{Ti}_3\text{C}_2\text{T}_x$ films annealed at temperatures ranging from 900 -1500 °C

under controlled He atmosphere using SPS while we held these temperatures for 1 h. We started with an *ex-situ* SPS experiment at 900 °C to compare the results with the *in-situ* heated XRD² results. The results for the single-flake (Figure 4a) and clay films (Figure 4b) annealed at 900 °C show faint (002) peaks at 8.87° and 8.59°, respectively, which correspond to $\text{Ti}_3\text{C}_2\text{T}_x$ *c*-LP of 19.94 Å and 20.59 Å, respectively. Similar to the *in-situ* hot stage XRD² results for 900 °C annealing for the single-flake film samples, a sharp peak at 36.26° and a peak at 77.07° can be attributed to the (111) and (222) peaks of TiC_y , and a peak at 17.99° corresponds to the (111) peak of Ti_2C (Figure 4a). In contrast, peaks corresponding to the Ti_2C (111) diffraction peak and the TiC_y (111), (200), (220), (311), and (222) are appeared for the $\text{Ti}_3\text{C}_2\text{T}_x$ clay film SPS annealed at 900 °C (Figure 4b). These results also indicate preferential formation of TiC_y and Ti_2C in the case of single-flake films and no preferential formation in the annealed clay films, which agrees with our *in-situ* hot stage XRD² annealing at 900 °C. Cross-sectional SEM shown in Figure 4c-d provides further support of this preferential vs. non-preferential formation, as the 900 °C single-flake film (Figure 4c) illustrates lamellar formation while the 900 °C clay film indicates cubic grain formation (Figure 4d).

After confirmation that the *ex-situ* SPS annealing similarly affected our $\text{Ti}_3\text{C}_2\text{T}_x$ films as *in-situ* hot stage XRD² annealed films at 900 °C, we investigated the phase transformation of these $\text{Ti}_3\text{C}_2\text{T}_x$ films at 1200 °C. In Figure 4a-b for the 1200 °C annealed single-flake and clay films, the peaks corresponding to $\text{Ti}_3\text{C}_2\text{T}_x$ are greatly diminished or no longer visible, which indicates that near-complete phase transformation of 2D $\text{Ti}_3\text{C}_2\text{T}_x$ to bulk 3D crystals. The XRD patterns of both single-flake and clay films annealed at 1200 °C show peaks correspond to the (111), (200), (220), (311), and (222) planes of TiC_y . The appearance of (200), (220) and (311)

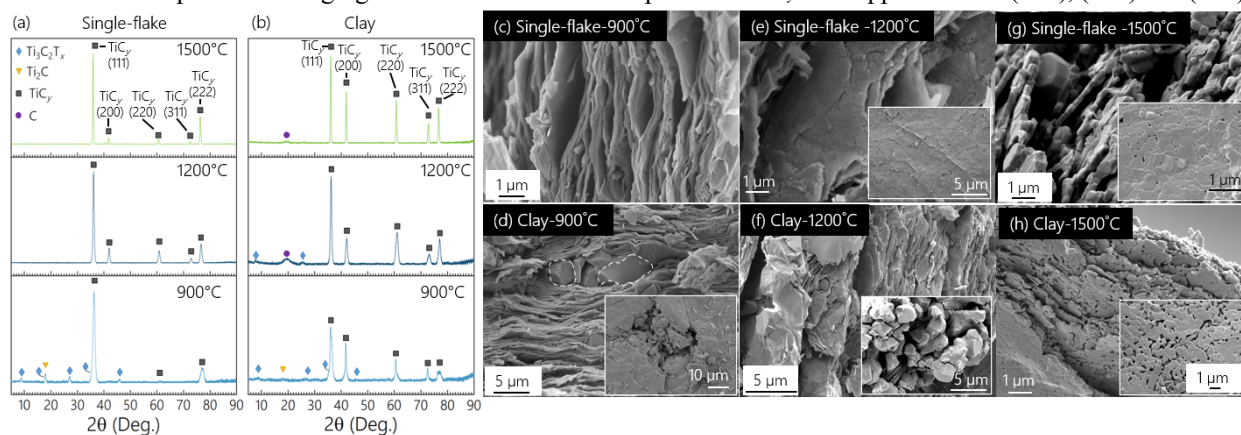


Figure 4. High temperature (900°C – 1500°C) annealing via SPS of both single-flake and clay $\text{Ti}_3\text{C}_2\text{T}_x$ films results in the bulk grain formation of TiC_y . XRD patterns of the annealed (a) single-flake and (b) clay films. Carbon peaks is due to the carbon tape used to setup the XRD² experiments and not a characteristic of the sample. (c) to (h) SEM images of the single-flake and clay films annealed at 900, 1200, and 1500 °C.

peaks in the single-flake film suggests non-preferential growth of TiC_y grains in single-flake films as the temperature is increased > 1000 °C. The (200), (220), and (311) peaks in the 1200 °C annealed single-flake film are less intense in comparison to those of the clay film (compare Figure 4a and b), which implies the partial preferential formation of cubic TiC_y grain in the single-flake film. For confirmation that these formed grains were indeed TiC_y , we conducted EDS analysis on these grains to confirm they are carbide grains and not oxides (Table S1). Comparison of the cross-section SEM of these two films in Figure 4e-f show that the 1200 °C annealed single-flake film retains some of its layered structure while the 1200°C annealed clay film is starting to appear mostly as cubic TiC_y grains.

As we increased the SPS annealing temperature to 1500 °C, the XRD patterns of the single-flake and clay films show no diffraction signal corresponding to $\text{Ti}_3\text{C}_2\text{T}_x$, which is in agreement with previous studies [27]. In these samples, we can only see peaks attributing to the (111), (200), (220), (311), and (222) diffraction peaks of cubic TiC_y . In addition, the TiC_y peaks are narrower with higher intensity in the films annealed at 1500 °C compare to those of the 1200 °C annealed films, which indicate the effect of high temperatures on the growth of cubic TiC_y grains. This growth of cubic TiC_y grains is verified in cross-section SEM images, as shown in Figure 4g-h. A possible explanation for the observance of large grain growth could be attributed to accelerated growth kinetics due to complete removal of surface groups from the MXene surface at temperature > 1100 °C [42]. While the XRD pattern of the 1500 °C annealed single-flake film show all five peaks of TiC_y , the (111) and (222) peaks still are higher in intensity than the other peaks which indicates partial preferred orientation of the resulting TiC_y even at 1500 °C as compared to non-preferential growth of TiC_y in 1500 °C annealed clay film. Cross-section SEM image in Figure 4g show the layered structure of the grains, which is in agreeance with our textured XRD and the results of a previous TEM study on annealed $\text{Ti}_3\text{C}_2\text{T}_x$ grains [42]. However, we note that the TiC_y crystals appear to grow more randomly in the 1500 °C annealed clay film (Figure 4h) as compared to the single-flake film (Figure 4g). Overall, XRD² data of 1200 °C and 1500 °C SPS annealed $\text{Ti}_3\text{C}_2\text{T}_x$ films shows a phase change to cubic TiC_y with no formation of superstructure 3D Ti_2C phases, which is in agreement with the phase diagram of nonstoichiometric Ti-C [45, 52] (Figure S1).

After analyzing the effects of annealing temperature on the resultant phase transformation of both $\text{Ti}_3\text{C}_2\text{T}_x$ single-flake and clay films, we then focused on a time-based characterization of the phase transformation of $\text{Ti}_3\text{C}_2\text{T}_x$ single-flake films at each temperature between

600 – 1000 °C through the use of *in-situ* hot stage XRD² with intermittent scans. An example plot of the XRD spectra at 800 °C at various annealing time points is shown in Figure 5a. Similar plots for 600, 700, 900, and 1000 °C *in-situ* hot stage XRD² scans are shown in Figure S9. It is important to note that the peak intensities of $\text{Ti}_3\text{C}_2\text{T}_x$ in the XRD spectra in Figure 5a and Figure S9 are lower when setup in our *in-situ* hot stage XRD² during the annealing experimentation. This is due to the protective graphite dome and running Ar gas which decrease the captured $\text{Ti}_3\text{C}_2\text{T}_x$ signal, as shown in Figure S10. However, the relative intensities of the $\text{Ti}_3\text{C}_2\text{T}_x$ peaks pre- and post-annealing (without the graphite dome and running Ar gas) can be seen in Figure S4.

Using our *in-situ* hot stage XRD² data, we first looked at how $\text{Ti}_3\text{C}_2\text{T}_x$ evolves during annealing at each temperature by characterizing the peak intensity of the (002) peak of samples annealed between 600–1000 °C over 2 h annealing time in Figure 5b. First, we utilized the 600 °C annealed XRD patterns as the control to see the effects of lower temperatures on the (002) peak of $\text{Ti}_3\text{C}_2\text{T}_x$. This was completed by dividing the intensity of the (002) peak at each time-step by its original peak intensity by counts (with dome and Ar gas). This analysis shows that the (002) peak, even in the 600 °C sample, decreases in intensity when annealed (Figure 5b). This could be due to the changes in stacking and distances of the $\text{Ti}_3\text{C}_2\text{T}_x$ flakes of 600 °C annealed $\text{Ti}_3\text{C}_2\text{T}_x$ films because of partial removal of its surface terminations, which would lead to less flake ordering and slightly disordered flake morphology due to annealing, as shown in the cross-sectional SEM in Figure S11. This increased disorder in the film may explain the result of the decreased intensity of the (002) peaks with respect to their original intensity. However, the 600 °C annealed $\text{Ti}_3\text{C}_2\text{T}_x$ film indicates a stable intensity around ~ 0.33 that of the original peak intensity. In our analysis, we used this ratio as the baseline for the determination of phase transformation of $\text{Ti}_3\text{C}_2\text{T}_x$.

Interestingly, the 700 °C annealed $\text{Ti}_3\text{C}_2\text{T}_x$ film averages around a similar value (~ 0.36 that of original peak intensity), which indicates that limited phase transformation takes place in $\text{Ti}_3\text{C}_2\text{T}_x$ when annealed at 700 °C. This confirms the stability of 2D $\text{Ti}_3\text{C}_2\text{T}_x$ at 600 °C and partial stability at 700 °C, which can be due to the effect of the surface groups on the prevention of phase transformation to Ti_2C or TiC_y . The slight increase in the intensity of the (002) $\text{Ti}_3\text{C}_2\text{T}_x$ peaks can be due to the increased removal of surface terminations, which would lead to increased ordering of the $\text{Ti}_3\text{C}_2\text{T}_x$ flakes [27]. However, $\text{Ti}_3\text{C}_2\text{T}_x$ films annealed at 800 – 1000 °C indicate a sharp decrease in peak intensity of the (002) peak, which clearly indicates the phase transformation of 2D $\text{Ti}_3\text{C}_2\text{T}_x$ to 3D crystalline Ti_2C and TiC_y phases at

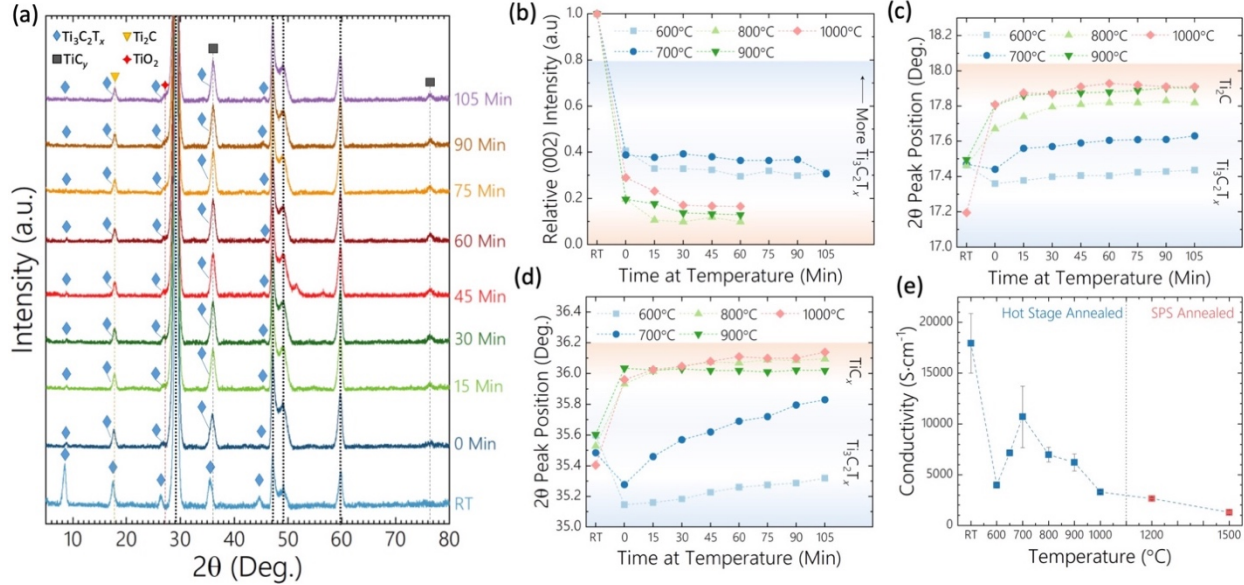


Figure 5. Time-dependent phase transformation of single-flake films of $\text{Ti}_3\text{C}_2\text{T}_x$ to Ti_2C and TiC_y at temperatures ranging from 600 – 1000 °C and its effect on the film conductive properties. (a) In-situ hot stage XRD² patterns of the a single-flake film annealed at 800 °C for 2 hours with intermittent scans every 15 minutes. (b) Relative (002) peak intensity of $\text{Ti}_3\text{C}_2\text{T}_x$ at different temperatures compare to its intensity before annealing. Analysis of the (002) peaks of the 800 – 1000 °C films are not shown as these peaks become unintelligible from the signal noise. (c) Peak position of the peak at 17.2°-17.9° 2 theta in the XRD patterns of the $\text{Ti}_3\text{C}_2\text{T}_x$ single-flake films during annealing. (d) Peak position of the peak at 35.2° to 36.1° (2θ) in the XRD patterns of the $\text{Ti}_3\text{C}_2\text{T}_x$ single-flake films during annealing at different temperatures. (e) Conductivity of the $\text{Ti}_3\text{C}_2\text{T}_x$ single-flake films annealed at different temperatures from 600 °C to 1500 °C.

these temperatures. This analysis can indicate that the phase transformation of 2D $\text{Ti}_3\text{C}_2\text{T}_x$ to bulk 3D crystalline phases takes place at temperatures of 800 – 1000 °C as compared to no phase transformation at 600 °C and small phase transformation at 700 °C during our annealing time.

Next, we analyzed the phase transformation of $\text{Ti}_3\text{C}_2\text{T}_x$ MXene to 3D Ti_2C through an investigation of the peak shifting of the most intense peak between 17.0 – 18.3° (2θ) from the (004) peak of 2D $\text{Ti}_3\text{C}_2\text{T}_x$ MXene to the (111) peak of 3D crystalline Ti_2C from 600-1000 °C as shown in Figure 5c. According to previous studies on $\text{Ti}_3\text{C}_2\text{T}_x$ MXene [27] and bulk titanium carbides [45], 600 °C is below a sufficient enough temperature to result in phase transformation of $\text{Ti}_3\text{C}_2\text{T}_x$ to TiC_y phases. Gusev *et.al.* predicted the phase transition of bulk 3D Ti_3C_2 to TiC_y and Ti_2C to begin occurring between 600 °C to 700 °C [45]. Using this analysis, we observed that the (004) peak of $\text{Ti}_3\text{C}_2\text{T}_x$ remains the most intense peak at 17.38° when annealed at 600 °C, which supports that $\text{Ti}_3\text{C}_2\text{T}_x$ does not undergo phase transformation at 600 °C in 2 h annealing. However, in accordance with Gusev’s analysis [45], the 700 °C annealed $\text{Ti}_3\text{C}_2\text{T}_x$ undergoes a similar decrease in peak position to 17.4° (2θ) before slowly increasing up to 17.6° (2θ) after 2 h of annealing. This supports that the $\text{Ti}_3\text{C}_2\text{T}_x$ film annealed at 700 °C

undergoes slowed transformation to Ti_2C , which is most likely due to the remaining surface terminations on the surface of $\text{Ti}_3\text{C}_2\text{T}_x$, which would slow the phase transformation of $\text{Ti}_3\text{C}_2\text{T}_x$ to other Ti-C phases. In addition, the most intense peak in the 17.0 – 18.3° (2θ) region quickly becomes the (111) peak of Ti_2C when $\text{Ti}_3\text{C}_2\text{T}_x$ is annealed at 800 – 1000 °C, which supports that temperatures of 800 °C or above is sufficient to cause quick phase transformation in $\text{Ti}_3\text{C}_2\text{T}_x$ MXene.

We also studied the phase transformation of 2D $\text{Ti}_3\text{C}_2\text{T}_x$ MXene to 3D crystalline TiC_y through investigation of the peak shifting of the most intense peak around 35.0 – 36.5° (2θ) from the (008) peak of $\text{Ti}_3\text{C}_2\text{T}_x$ to the (111) peak of TiC_y . Figure 5d illustrates that at 600 °C the (008) peak position of $\text{Ti}_3\text{C}_2\text{T}_x$ shifts down to 35.32° (2θ), which does not correspond to the formation of TiC_y . In addition, the 700 °C peak shows slow phase transformation via an initial decrease in peak position to 35.49° (2θ) before slowly increasing up to 35.83° (2θ) after 2 h of annealing. This indicates that $\text{Ti}_3\text{C}_2\text{T}_x$ heated at 600 °C is unlikely to undergo phase transformation to TiC_y while 700 °C annealing will initiate slow phase transition. However, samples annealed from 800 – 1000 °C display quick peak shifting to peak positions between 36.02 - 36.14° (2θ), which corresponds to TiC_y (111) peak.

In order to understand these results on the slowed transformation of 700 °C – 2 h annealed $Ti_3C_2T_x$ to TiC_y , we compared them to the previous studies on bulk titanium carbides. Although previous studies [45] on the phase transition of bulk titanium carbides indicated that 700 °C should result in full phase transformation to TiC_y , our slow shifting of the most intense peak between 35 - 36° (2 θ) does not indicate this transformation in 2 h of annealing. The slow shifting of the 700 °C in comparison to the 800 – 1000 °C peaks could be attributed to the effects of slower kinetics at 700 °C [71]. It is also possible that at longer times complete phase transformation does not occur, possibly due to the effect of still present –F surface terminations on the surface of $Ti_3C_2T_x$ [27, 39, 41, 42] as previously mentioned in the discussion of the changing *a*-LP and crystallite size of TiC_y and Ti_2C . Further studies on long duration annealing of $Ti_3C_2T_x$ are needed to understand the phase equilibrium of single-flake $Ti_3C_2T_x$ MXene at 700 °C.

We next analyzed the effect of this phase transformation on the electrical conductivity of the annealed (600 – 1500 °C) $Ti_3C_2T_x$ films (Figure 5e). The electrical conductivity of single-flake films show a decrease in conductivity values with an increase in annealing temperatures. Single-flake $Ti_3C_2T_x$ films after overnight annealing at 150 °C exhibited conductivity of $\sim 17000 \pm 274 \text{ S}\cdot\text{cm}^{-1}$. A drop in conductivity was observed for samples annealed at 600 °C with the values increasing for 700 °C, and gradually decreasing for samples annealed at 800 and 900 °C. A subsequent drop in conductivity is observed for films annealed at 1000, 1200, and 1500 °C. A complete table of the electrical conductivity results is given in Table S2. The rise in conductivity of the films at 700 °C may be attributed to increased ordering of the $Ti_3C_2T_x$ sheets due to loss of structural water molecules along with the loss of –OH and –F functional groups from the surface layer of $Ti_3C_2T_x$ flakes in tandem with little phase transformation to Ti_2C or TiC_y . Carbon vacancy order to disorder phase transformation can also play a role in the decrease in electrical conductivity at higher temperatures. In general, ordering of carbon vacancies in transition metal carbides have been shown to exhibit improved properties, such as higher hardness and electrical conductivity, in comparison to their disordered phases [50, 72, 73]. In the *disordered* carbon vacancy transition metal carbides, the electrical conductivity decreases with a decrease in the carbon content due to the increase of the scattering rate of conduction electrons on point defects [60]. However, we suspect that the decrease in electrical conductivity in our experiments could also be due to growth of randomly formed and randomly oriented polycrystalline grains of TiC_y , likely with little interconnection between different grains. Although this study illustrated a decrease due to high temperature annealing, future studies with more

control of the grain growth of TiC_y crystals could possibly see an improved electrical conductivity past that of $Ti_3C_2T_x$ MXene.

Conclusion

In this study, we experimentally studied the stability and phase transformations in $Ti_3C_2T_x$ MXene due to high temperature annealing under controlled environments, using *in-situ* hot stage XRD², tube furnace and SPS techniques. Our *in-situ* hot stage XRD² analysis showed that $Ti_3C_2T_x$ MXene keeps its 2D layered structure up to 600 °C, after which 3D crystalline phases of Ti-C are formed. Formation of stable 3D crystalline Ti_2C and TiC_y phases up to annealing temperatures of 1000 °C in both single-flake films and multi-layer clay films of MXene with subsequent transition to cubic TiC_y above 1000 °C are indicative of MXene's potential to be introduced as a competent carbide material for high-temperature applications.

We further observed that the morphology of the resulting 3D crystalline TiC_y depends on the initial MXene morphology, as annealing the delaminated $Ti_3C_2T_x$ single-flake films results in TiC_y grains with preferred orientation and lamellar grains. However, annealing the multi-layer $Ti_3C_2T_x$ in the clay films makes 3D crystals with no preferred orientation. Future applications of MXene as a nano-lamellar 2D nanomaterial in high temperature applications requires a fundamental understanding of the stability of MXene in high temperature environments. Our study lays the groundwork for future investigation of the use of this high-temperature nanomaterial in future energy storage, catalytic, and composite applications which will continue to make this promising 2D material an ideal candidate to meet many of the technological demands of tomorrow.

Acknowledgments

The authors acknowledge startup funding from the Department of Mechanical and Energy Engineering and Purdue School of Engineering and Technology at IUPUI. BZ acknowledges the support from Henan Key Laboratory of Photovoltaic Materials, Henan University, Kaifeng, China. We would also like to acknowledge the use of JEOL7800f Field Emission Scanning Electron Microscope, which was awarded through NSF grant MRI-1229514, and for use of Bruker XRD equipment, which was awarded through NSF grant MRI-1429241.

The authors declare no competing financial interests.

References

- [1] K. Koski, Cui, Y., The New Skinny in Two-Dimensional Nanomaterials, *ACS Nano*, 7 (2013) 3739–3743.
- [2] H. Jin, C. Guo, X. Liu, J. Liu, A. Vasileff, Y. Jiao, Y. Zheng, S.Z. Qiao, Emerging Two-Dimensional Nanomaterials for Electrocatalysis, *Chem Rev*, 118 (2018) 6337–6408.
- [3] L. Dai, Functionalization of Graphene for Efficient Energy Conversion and Storage, *Accounts of Chemical Research*, 46 (2012).
- [4] X. Peng, L. Peng, C. Wu, Y. Xie, Two dimensional nanomaterials for flexible supercapacitors, *Chem Soc Rev*, 43 (2014) 3303–3323.
- [5] M.F. El-Kady, Y. Shao, R.B. Kaner, Graphene for batteries, supercapacitors and beyond, *Nature Reviews Materials*, 1 (2016).
- [6] Y. Wang, J. Mao, X. Meng, L. Yu, D. Deng, X. Bao, Catalysis with Two-Dimensional Materials Confining Single Atoms: Concept, Design, and Applications, *Chem Rev*, 119 (2019) 1806–1854.
- [7] Y. Chen, K. Yang, B. Jiang, J. Li, M. Zeng, L. Fu, Emerging two-dimensional nanomaterials for electrochemical hydrogen evolution, *Journal of Materials Chemistry A*, 5 (2017) 8187–8208.
- [8] M. Naguib, M. Kurtoglu, V. Presser, J. Lu, J. Niu, M. Heon, L. Hultman, Y. Gogotsi, M.W. Barsoum, Two-dimensional nanocrystals produced by exfoliation of Ti_3AlC_2 , *Adv Mater*, 23 (2011) 4248–4253.
- [9] M. Naguib, Mashtalir, O., Carle, J., Presser, V., Lu, J., Hultman, L., Gogotsi, Y., Barsoum, M.W., Two-Dimensional Transition Metal Carbides, *ACS Nano*, 6 (2012) 1322–1331.
- [10] M.A. Hope, A.C. Forse, K.J. Griffith, M.R. Lukatskaya, M. Ghidui, Y. Gogotsi, C.P. Grey, NMR reveals the surface functionalisation of Ti_3C_2 MXene, *Phys Chem Chem Phys*, 18 (2016) 5099–5102.
- [11] Y. Li, H. Shao, Z. Lin, J. Lu, L. Liu, B. Duployer, P.O.A. Persson, P. Eklund, L. Hultman, M. Li, K. Chen, X.H. Zha, S. Du, P. Rozier, Z. Chai, E. Raymundo-Pinero, P.L. Taberna, P. Simon, Q. Huang, A general Lewis acidic etching route for preparing MXenes with enhanced electrochemical performance in non-aqueous electrolyte, *Nat Mater*, 19 (2020) 894–899.
- [12] M. Sokol, V. Natu, S. Kota, M.W. Barsoum, On the Chemical Diversity of the MAX Phases, *Trends in Chemistry*, 1 (2019) 210–223.
- [13] M. Ghidui, Lukatskaya, M.R., Zhao, M.Q., Gogotsi, Y., Barsoum, M.B., Conductive two-dimensional titanium carbide ‘clay’ with high volumetric capacitance, *Nature*, 516 (2014) 78–81.
- [14] M. Alhabeb, K. Maleski, B. Anasori, P. Lelyukh, L. Clark, S. Sin, Y. Gogotsi, Guidelines for Synthesis and Processing of Two-Dimensional Titanium Carbide ($\text{Ti}_3\text{C}_2\text{T}_x$ MXene), *Chemistry of Materials*, 29 (2017) 7633–7644.
- [15] B. Anasori, M.R. Lukatskaya, Y. Gogotsi, 2D metal carbides and nitrides (MXenes) for energy storage, *Nature Reviews Materials*, 2 (2017).
- [16] K.R.G. Lim, A.D. Handoko, S.K. Nemani, B. Wyatt, H.Y. Jiang, J. Tang, B. Anasori, Z.W. Seh, Rational Design of Two-Dimensional Transition Metal Carbide/Nitride (MXene) Hybrids and Nanocomposites for Catalytic Energy Storage and Conversion, *ACS Nano*, (2020).
- [17] T. Mathis, Maleski, K., Goad, A., Sarycheva, A., Anayee, M., Foucher, A.C., Hantanasirisakul, K., Stach, E., Gogotsi, Y., Modified MAX Phase Synthesis for Environmentally Stable and Highly Conductive Ti_3C_2 MXene, *ChemRxiv*, (2020).
- [18] X. Liang, A. Garsuch, L.F. Nazar, Sulfur cathodes based on conductive MXene nanosheets for high-performance lithium-sulfur batteries, *Angew Chem Int Ed Engl*, 54 (2015) 3907–3911.
- [19] A. Lipatov, Lu, H., Alhabeb, M., Anasori, B., Gruverman, A., Gogotsi, Y., Sinitskii, A., Elastic properties of 2D $\text{Ti}_3\text{C}_2\text{T}_x$ MXene monolayers and bilayers, *Sci Adv*, 4 (2018) 1–7.
- [20] A. Lipatov, M. Alhabeb, H. Lu, S. Zhao, M.J. Loes, N.S. Vorobeve, Y. Dall’Agnese, Y. Gao, A. Gruverman, Y. Gogotsi, A. Sinitskii, Electrical and Elastic Properties of Individual Single-Layer $\text{Nb}_4\text{C}_3\text{T}_x$ MXene Flakes, *Advanced Electronic Materials*, (2020).
- [21] H. Huang, J. Cui, G. Liu, R. Bi, L. Zhang, Carbon-Coated MoSe_2 /MXene Hybrid Nanosheets for Superior Potassium Storage, *ACS Nano*, 13 (2019) 3448–3456.
- [22] C. Cheng, X. Zhang, Z. Fu, Z. Yang, Strong metal-support interactions impart activity in the oxygen reduction reaction: Au monolayer on Mo_2C (MXene), *J Phys Condens Matter*, 30 (2018) 475201.
- [23] Y. Gogotsi, B. Anasori, The Rise of MXenes, *ACS Nano*, 13 (2019) 8491–8494.
- [24] J. Zhang, N. Kong, S. Uzun, A. Levitt, S. Seyedin, P.A. Lynch, S. Qin, M. Han, W. Yang, J. Liu, X. Wang, Y. Gogotsi, J.M. Razal, Scalable Manufacturing of Free-Standing, Strong $\text{Ti}_3\text{C}_2\text{T}_x$ MXene Films with Outstanding Conductivity, *Adv Mater*, (2020) e2001093.
- [25] Z. Ling, C.E. Ren, M.Q. Zhao, J. Yang, J.M. Giammarco, J. Qiu, M.W. Barsoum, Y. Gogotsi, Flexible and conductive MXene films and nanocomposites with high capacitance, *Proc Natl Acad Sci U S A*, 111 (2014) 16676–16681.
- [26] K. Maleski, V.N. Mochalin, Y. Gogotsi, Dispersions of Two-Dimensional Titanium Carbide MXene in Organic Solvents, *Chemistry of Materials*, 29 (2017) 1632–1640.
- [27] M. Seredych, C.E. Shuck, D. Pinto, M. Alhabeb, E. Precetti, G. Deysher, B. Anasori, N. Kurra, Y. Gogotsi, High-Temperature Behavior and Surface Chemistry of Carbide MXenes Studied by Thermal Analysis, *Chem. Mater.*, 31 (2019) 3324–3332.
- [28] F. Xia, J. Lao, R. Yu, X. Sang, J. Luo, Y. Li, J. Wu, Ambient oxidation of Ti_3C_2 MXene initialized by atomic defects, *Nanoscale*, 11 (2019) 23330–23337.
- [29] R. Lotfi, M. Naguib, D.E. Yilmaz, J. Nanda, A.C.T. van Duin, A comparative study on the oxidation of two-dimensional Ti_3C_2 MXene structures in different environments, *Journal of Materials Chemistry A*, 6 (2018) 12733–12743.
- [30] S. Huang, V.N. Mochalin, Hydrolysis of 2D Transition-Metal Carbides (MXenes) in Colloidal Solutions, *Inorg Chem*, 58 (2019) 1958–1966.
- [31] C.J. Zhang, S. Pinilla, N. McEvoy, C.P. Cullen, B. Anasori, E. Long, S.-H. Park, A. Seral-Ascaso, A. Shmeliov, D. Krishnan, C. Morant, X. Liu, G.S. Duesberg, Y. Gogotsi, V. Nicolosi, Oxidation Stability of Colloidal Two-Dimensional Titanium Carbides (MXenes), *Chemistry of Materials*, 29 (2017) 4848–4856.
- [32] Y. Xie, M. Naguib, V.N. Mochalin, M.W. Barsoum, Y. Gogotsi, X. Yu, K.W. Nam, X.Q. Yang, A.I. Kolesnikov, P.R. Kent, Role of surface structure on Li-ion energy storage capacity of two-dimensional transition-metal carbides, *J Am Chem Soc*, 136 (2014) 6385–6394.
- [33] M. Naguib, O. Mashtalir, M.R. Lukatskaya, B. Dyatkin, C. Zhang, V. Presser, Y. Gogotsi, M.W. Barsoum, One-step synthesis of nanocrystalline transition metal oxides on thin sheets of disordered graphitic carbon by oxidation of MXenes, *Chem Commun (Camb)*, 50 (2014) 7420–7423.
- [34] Y. Fang, Z. Liu, J. Han, Z. Jin, Y. Han, F. Wang, Y. Niu, Y. Wu, Y. Xu, High-Performance Electrocatalytic Conversion of N_2 to NH_3 Using Oxygen-Vacancy-Rich TiO_2 In Situ Grown on $\text{Ti}_3\text{C}_2\text{T}_x$ MXene, *Advanced Energy Materials*, 9 (2019).
- [35] V. Kamysbayev, N.M. James, A.S. Filatov, V. Srivastava, B. Anasori, H.M. Jaeger, Y. Gogotsi, D.V. Talapin, Colloidal Gelation in Liquid Metals Enables Functional Nanocomposites of 2D Metal Carbides (MXenes) and Lightweight Metals, *ACS Nano*, (2019).
- [36] M. Fei, R. Lin, Y. Lu, X. Zhang, R. Bian, J. Cheng, P. Luo, C. Xu, D. Cai, MXene-reinforced alumina ceramic composites, *Ceram. Int.*, 43 (2017) 17206–17210.
- [37] J. Guo, B. Legum, B. Anasori, K. Wang, P. Lelyukh, Y. Gogotsi, C.A. Randall, Cold Sintered Ceramic Nanocomposites of 2D MXene and Zinc Oxide, *Adv Mater*, 30 (2018) e1801846.
- [38] J. Hu, S. Li, J. Zhang, Q. Chang, W. Yu, Y. Zhou, Mechanical properties and frictional resistance of Al composites reinforced with $\text{Ti}_3\text{C}_2\text{T}_x$ MXene, *Chinese Chemical Letters*, (2019).

- [39] J.L. Hart, K. Hantanasirisakul, A.C. Lang, B. Anasori, D. Pinto, Y. Pivak, J.T. van Omme, S.J. May, Y. Gogotsi, M.L. Taheri, Control of MXenes' electronic properties through termination and intercalation, *Nat Commun*, 10 (2019) 522.
- [40] R.B. Rakhi, B. Ahmed, M.N. Hedhili, D.H. Anjum, H.N. Alshareef, Effect of Postetch Annealing Gas Composition on the Structural and Electrochemical Properties of Ti_2CT_x MXene Electrodes for Supercapacitor Applications, *Chemistry of Materials*, 27 (2015) 5314-5323.
- [41] I. Persson, L.-Å. Näslund, J. Halim, M.W. Barsoum, V. Darakchieva, J. Palisaitis, J. Rosen, P.O.Å. Persson, On the organization and thermal behavior of functional groups on Ti_3C_2 MXene surfaces in vacuum, *2D Materials*, 5 (2017) 015002.
- [42] B. Ji, S. Fan, X. Ma, K. Hu, L. Wang, C. Luan, J. Deng, L. Cheng, L. Zhang, Electromagnetic shielding behavior of heat-treated $Ti_3C_2T_x$ MXene accompanied by structural and phase changes, *Carbon*, 165 (2020) 150-162.
- [43] X. Sang, Y. Xie, D.E. Yilmaz, R. Lotfi, M. Alhabeab, A. Ostadhossein, B. Anasori, W. Sun, X. Li, K. Xiao, P.R.C. Kent, A.C.T. van Duin, Y. Gogotsi, R.R. Unocic, In situ atomistic insight into the growth mechanisms of single layer 2D transition metal carbides, *Nat Commun*, 9 (2018) 2266.
- [44] G.M. Demyashev, Transition metal-based nanolamellar phases, *Progress in Materials Science*, 55 (2010) 629-674.
- [45] A.I. Gusev, Phase equilibria, phases and compounds in the Ti-C system, *Russian Chemical Reviews*, 71 (2002) 439-463.
- [46] V. Moisy-Maurice, N. Lorenzelli, C. De Novion, P. Convert, High temperature neutron diffraction study of the order-disorder transition in TiC_{1-x} , *Acta Metallurgica*, 30 (1982) 1769-1779.
- [47] C.-H. de Novion, J. Landesman, Order and disorder in transition metal carbides and nitrides: experimental and theoretical aspects, *Pure and Applied Chemistry*, 57 (1985) 1391-1402.
- [48] A.I. Gusev, A.S. Kurlov, V.N. Lipatnikov, Atomic and vacancy ordering in carbide ζ - Ta_xC_{3-x} ($0.28 \leq x \leq 0.40$) and phase equilibria in the Ta-C system, *Journal of Solid State Chemistry*, 180 (2007) 3234-3246.
- [49] N. Lorenzelli, R. Caudron, J. Landesman, C. De Novion, Influence of the ordering of carbon vacancies on the electronic properties of $TiC_{0.625}$, *Solid state communications*, 59 (1986) 765-769.
- [50] L.V.Z. V. N. Lipatnikov, A. I. Gusev, Disorder-order phase transformations and electrical resistivity of nonstoichiometric titanium carbide, *Physics of the Solid State*, 40 (1998).
- [51] A.I.G. V. N. Lipatnikov, Effect of ordering on the structure and specific heat of nonstoichiometric titanium carbide, *JETP Letters*, 69 (1999) 669-675.
- [52] A.K. V. N. Lipatnikov, L. V. Zueva, A. I. Gusev, Ordering Effects in Nonstoichiometric Titanium Carbide, *Inorganic Materials*, 36 (2000) 155-161.
- [53] H. Goretzki, Neutron Diffraction Studies on Titanium-Carbon and Zirconium-Carbon Alloys, *Physica Status Solidi (b)*, 20 (1967) K141-K143.
- [54] N. Lorenzelli, R. Caudron, J. Landesman, C. De Novion, Influence of the ordering of carbon vacancies on the electronic properties of $TiC_{0.625}$, *Solid State Commun*, 59 (1986) 765-769.
- [55] P.A. Korzhavyi, L.V. Pourovskii, H.W. Hugosson, A.V. Ruban, B. Johansson, Ab initio study of phase equilibria in TiC_x , *Phys. Rev. Lett.*, 88 (2001) 015505.
- [56] A. Gusev, A. Rempel, Atomic ordering and phase equilibria in strongly nonstoichiometric carbides and nitrides, in: Y. Gogotsi, R.A. Andrievski (Eds.) *Materials Science of Carbides, Nitrides and Borides*, Springer, 1999, pp. 47-64.
- [57] V. Lipatnikov, A. Rempel, A. Gusev, Atomic Ordering and Hardness of Nonstoichiometric Titanium Carbide, *Int. J. of Refractory Metals & Hard Materials*, 15 (1997) 61-64.
- [58] N.V. Dzhilabadzhe, Maysuradzhe, B.G., Kuteliya, E.R, On structure of crystalline phases in thin Ti-C films, *Fizika Metallov | Metallovedenie*, 86 (1998) 85-92.
- [59] V. Lipatnikov, A. Rempel, A. Gusev, Atomic ordering and hardness of nonstoichiometric titanium carbide, *International Journal of Refractory Metals and Hard Materials*, 15 (1997) 61-64.
- [60] L. Dy, W.S. Williams, Resistivity, superconductivity, and order-disorder transformations in transition metal carbides and hydrogen-doped carbides, *Journal of Applied Physics*, 53 (1982) 8915-8927.
- [61] A. Gusev, Disorder and Long-Range Order in Non-Stoichiometric Interstitial Compounds Transition Metal Carbides, Nitrides, and Oxides, *Physica status solidi (b)*, 163 (1991) 17-54.
- [62] V.N. Lipatnikov, L.V. Zueva, A.I. Gusev, A. Kottar, Disorder-order phase transformations and electrical resistivity of nonstoichiometric titanium carbide, *Physics of the Solid State*, 40 (1998) 1211-1218.
- [63] A.P. Asia Sarycheva, Yuqiao Liu, Kapil Dandekar, Babak Anasori, Yury Gogotsi, 2D titanium carbide (MXene) for wireless communication, *Sci Adv*, 4 (2018) 1-8.
- [64] K.D. Fredrickson, B. Anasori, Z.W. Seh, Y. Gogotsi, A. Vojvodic, Effects of Applied Potential and Water Intercalation on the Surface Chemistry of Ti_2C and Mo_2C MXenes, *The Journal of Physical Chemistry C*, 120 (2016) 28432-28440.
- [65] M. Ghidui, M.W. Barsoum, The $\{110\}$ reflection in X-ray diffraction of MXene films: Misinterpretation and measurement via non-standard orientation, *Journal of the American Ceramic Society*, 100 (2017) 5395-5399.
- [66] B.-X. Dong, H.-Y. Yang, F. Qiu, Q. Li, S.-L. Shu, B.-Q. Zhang, Q.-C. Jiang, Design of TiC nanoparticles and their morphology manipulating mechanisms by stoichiometric ratios: Experiment and first-principle calculation, *Materials & Design*, 181 (2019).
- [67] S.A. Kazemi, Y. Wang, Super strong 2D titanium carbide MXene-based materials: a theoretical prediction, *J Phys Condens Matter*, 32 (2020) 11LT01.
- [68] A. Jain, S.P. Ong, G. Hautier, W. Chen, W.D. Richards, S. Dacek, S. Cholia, D. Gunter, D. Skinner, G. Ceder, K.A. Persson, Commentary: The Materials Project: A materials genome approach to accelerating materials innovation, *APL Materials*, 1 (2013).
- [69] A.I.G. L. V. Zueva, Effect of nonstoichiometry and ordering on the period of the basis structure of cubic titanium carbide, *Physics of the Solid State*, 41 (1999) 1032-1038.
- [70] V. Kamysbayev, Filatov, A.S., Hu, H., Rui, X., Lagunas, F., Wang, D., Klie, R.F., Talapin, D.V., Covalent surface modifications and superconductivity of two-dimensional metal carbide MXenes, *Science*, (2020).
- [71] D.W.R. S.D. Dunmead, C. E. Semle, J. Birch Holt, Kinetics of Combustion Synthesis in the Ti-C and Ti-C-Ni Systems, *J. Am. Ceram. Soc.*, 72 (1989) 2318-2324.
- [72] V. Lipatnikov, W. Lengauer, P. Ettmayer, E. Keil, G. Groboth, E. Kny, Effects of vacancy ordering on structure and properties of vanadium carbide, *Journal of alloys and compounds*, 261 (1997) 192-197.
- [73] D. Rafaja, W. Lengauer, P. Ettmayer, V. Lipatnikov, Rietveld analysis of the ordering in V_8C_7 , *Journal of alloys and compounds*, 269 (1998) 60-62.